



Interface Modification of Sputtered NiO_x as the Hole-Transporting Layer for Efficient Inverted Planar Perovskite Solar Cells

| | |
|-------------------------------|---|
| Journal: | <i>Journal of Materials Chemistry C</i> |
| Manuscript ID | TC-ART-10-2019-005759.R1 |
| Article Type: | Paper |
| Date Submitted by the Author: | 10-Dec-2019 |
| Complete List of Authors: | Zheng, Xiaolu; Wuhan University Song, Zhaoning; University of Toledo, Physics and Astronomy Chen, Zhiliang; Wuhan University Bista, Sandip ; University of Toledo Gui, Pengbin; Wuhan University Shrestha, Niraj; University of Toledo, Physics and Astronomy Chen, Cong; University of Toledo Li, Chongwen; University of Toledo Yin, Xingxin; University of Toledo Awni, Rasha; University of Toledo Lei, Hongwei; Huazhong Agricultural University Chen, Tao; Wuhan University Ellingson, Randy; University of Toledo Yan, Yanfa; University of Toledo, Physics and Astronomy Fang, Guojia; Wuhan University |
| | |

Interface Modification of Sputtered NiO_x as the Hole-Transporting Layer for Efficient Inverted Planar Perovskite Solar Cells

Xiaolu Zheng,^{†, [a], [b], [d]} Zhaoning Song,^{†,*, [b]} Zhiliang Chen,^{†, [a]} Sandip Singh Bista,^[b] Pengbin Gui,^[a] Niraj Shrestha,^[b] Cong Chen,^{[a], [b]} Chongwen Li,^[b] Xinxing Yin,^[b] Rasha A. Awni,^[b] Hongwei Lei,^[c] Chen Tao,^[a] Randy J. Ellingson,^[b] Yanfa Yan,^[b] Guojia Fang^{*, [a], [d]}

[a] Key Lab of Artificial Micro- and Nano-Structures of Ministry of Education of China, School of Physics and Technology, Wuhan University, Wuhan 430072, P. R. China
Email: gjfang@whu.edu.cn

[b] Department of Physics and Astronomy and Wright Center for Photovoltaics Innovation and Commercialization, The University of Toledo, Toledo, OH, 43606, United States
Email: zhaoning.song@utoledo.edu

[c] College of Science, Huazhong Agricultural University, Wuhan 430070, P. R. China

[d] Shenzhen Institute, Wuhan University, Shenzhen 518055, P. R. China.

[†] These authors contributed equally.

Abstract

Nickel oxide (NiO_x) as hole-transporting layer (HTL) in perovskite solar cells (PSCs) has been studied extensively in recent years. However, unlike the solution-processed NiO_x films, magnetron sputtered NiO_x exhibits relatively low conductivity and imperfect band alignment with perovskites, severely limiting the device performance of PSCs. In this study, a synergistically combined strategy consisting of triple interface treatments — including post-annealing, O₂-plasma, and potassium chloride treatments — is employed to modulate the optoelectronic properties of the

sputtered NiO_x films. Through this approach, we successfully obtain NiO_x films with increased carrier density and conductivity, better energy level alignment with the perovskite absorber layer, reduced interface trap density, and improved interfacial charge extraction. PSCs using this modified sputtered NiO_x as the HTL deliver a highest stabilized efficiency of 18.7%. Our result offers an alternative method to manipulate sputtered NiO_x thin film properties and thereby sheds the light on a manufacturing pathway to perovskite solar cells featuring sputtered NiO_x HTL.

Introduction

Perovskite solar cells (PSCs) have attracted tremendous attention due to their excellent photovoltaic properties¹⁻³ and rapid increasing power conversion efficiencies (PCEs)⁴. Nickel oxide (NiO_x) as an intrinsic p-type semiconductor is considered to be a potential low-cost candidate for stable hole-transporting layer (HTL) in inverted p-i-n structure PSCs owing to its wide band gap, well-aligned valence band edge, and appropriate electrical properties⁵⁻⁸. Diverse deposition methods have been adopted to fabricate NiO_x HTLs, including solution-based methods, such as nanoparticle⁹⁻¹¹, sol-gel⁷, solution-combustion route¹², and electrochemical deposition¹³, and vacuum-based approaches, including magnetron sputtering^{6, 14, 15}, atomic layer deposition¹⁶, pulsed laser deposition¹⁷, and electron beam evaporation¹⁸. Among these methods, magnetron sputtering is more favorable in industry due to its high compatibility, low cost, large-scale applicability, and universality for flat and textured substrates. While PSCs with the solution-processed NiO_x HTLs have demonstrated PCEs over 20%^{9, 12, 19}, devices with the sputtered NiO_x have typically suffered from less competitive PCEs below 18.5%⁶. The relatively low conductivity and imperfect band alignment with the perovskite absorber layers are considered to be the main hurdles in obtaining good device performances for sputtered NiO_x-based PSCs^{14, 20, 21}.

Many efforts have been devoted to improving the optoelectronic properties of NiO_x films. Lattice doping is conventionally adopted to ameliorate the electrical properties of solution-processed NiO_x films^{9, 22-24}. However, this strategy encounters some obstacles when preparing sputtered NiO_x. For example, co-sputtering deposition

is subject to complicated parameter control and limited element selection^{6, 25}, and thus has rarely been explored. Alternatively, interface modification has been employed in both electron-transporting layers (ETLs) and HTLs to achieve better device performance and stability²⁶⁻²⁹. Ratcliff *et al.*³⁰ discovered that the O₂-plasma treatment on the NiO_x film increased its work function (WF) and decreased the midgap states close to its valence band edge. Chen *et al.*¹⁹ demonstrated that the alkali chloride interfacial layer could improve the ordering of the atop perovskite layer and hence reduced defect density and interfacial recombination. Although most interface treatments were done on solution-processed NiO_x films, these strategies are in fact also suitable for the sputtered ones due to their good usability and maneuverability.

In this work, we demonstrated that appropriate interface treatments modify the optoelectronic properties of the sputtered NiO_x films. Through the synergistic combination of three interface treatments, namely, post-annealing, O₂-plasma, and potassium chloride (KCl) passivation, we successfully increased the carrier density of the sputtered NiO_x films, adjusted the surface work function, reduced the interfacial trap density, and improved charge extraction at the interface. As a result, PSCs with the optimally modified NiO_x HTL delivered a PCE of 19.16% with the reversed voltage scan and a steady state efficiency (SSE) of 18.7%, approximately 25% efficiency enhancement compared to the ones with the as-sputtered NiO_x. Our results prove the feasibility of the interface treatment in enhancing PSCs performance with sputtered NiO_x HTL.

Results and discussion

We first characterized the structural and optoelectronic properties of NiO_x thin films prepared by radio frequency (RF) magnetron sputtering with a NiO target. The top-view scanning electron microscopy (SEM) image shown in **Figure 1(a)** reveals the dense and uniform surface of the as-sputtered NiO_x film with an average crystallite size of ~10 nm. Grazing incidence X-ray diffraction (GIXRD) measurement of the NiO_x film deposited on a glass substrate shows the cubic crystal structure of NiO with characteristic peaks located at ~ 37°, 43° and 63°, corresponding to the (111), (200),

and (220) plane, respectively (**Figure 1(b)**). The optical band gap (E_g) of the NiO_x film is determined to be 3.63 eV by the Tauc plot from the UV-vis spectroscopy measurement (**Figure 1(c)**), consistent with the values reported in the literature^{31, 32}. The Fermi energy level (E_F) and valence band maximum (E_{VBM}) of the as-sputtered NiO_x measured by ultraviolet photoelectron spectroscopy (UPS) are 4.85 and 5.35 eV, respectively (**Figure 1(d)**). The appropriate energy level matches to indium tin oxide (ITO) and perovskites (**Figure 1(e)** and **Table S1**) make the as-sputtered NiO_x an ideal HTL for PSCs in the inverted (or p-i-n) configuration (**Figure 1(f)**).

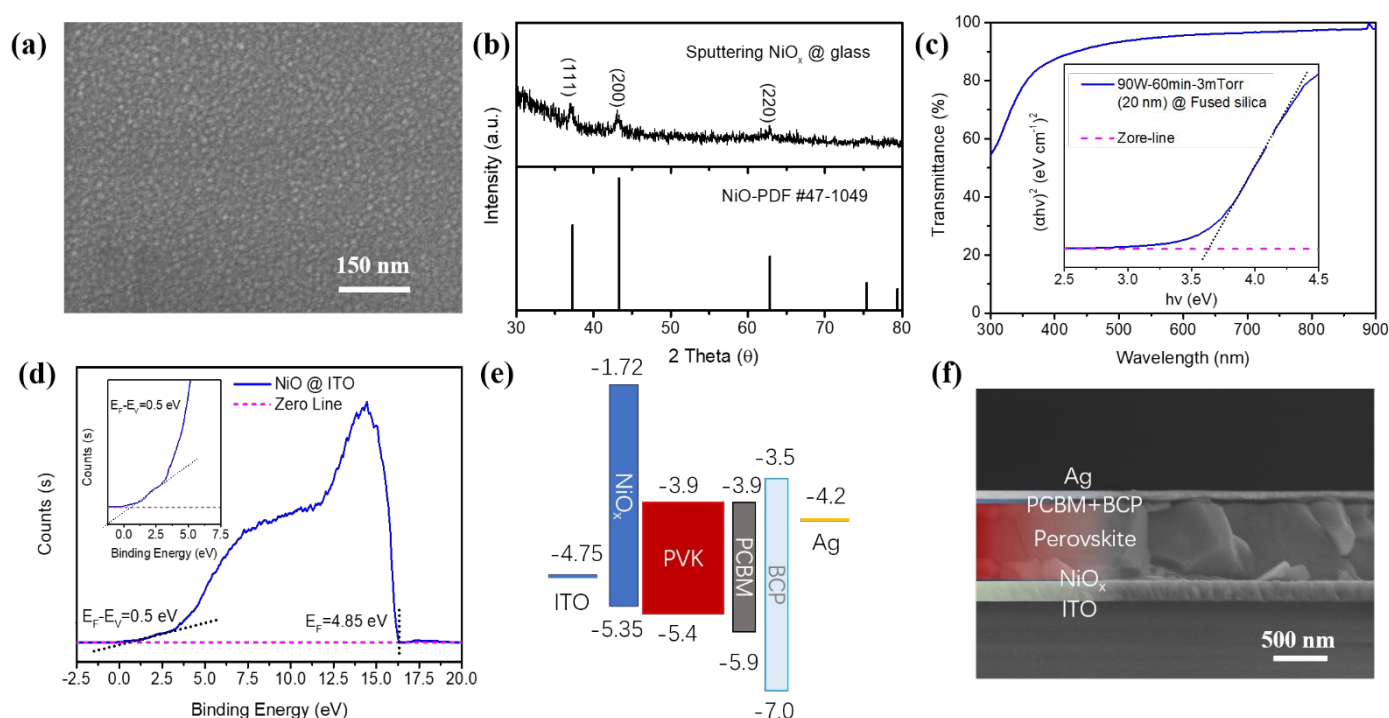


Figure 1. (a) Top-view SEM image of an as-sputtered NiO_x film deposited on a silicon substrate. (b) GIXRD pattern of an as-sputtered NiO_x film deposited on a glass substrate. (c) Transmission spectrum of an as-sputtered NiO_x film with a thickness of 20 nm and its corresponding Tauc plot. (d) UPS spectrum of an as- NiO_x film deposited on an ITO coated glass substrate. Inset shows the magnified image of the low binding energy onset. (e) Schematic of the energy diagram and (f) Cross-sectional SEM image of PSCs with the structure of ITO/ NiO_x /perovskite/PCBM/BCP/Ag.

To test the feasibility of the as-sputtered NiO_x as the HTL in PSCs, we fabricated inverted PSCs with a structure of ITO/ NiO_x /perovskite/phenyl-C61-butyric acid methyl

ester (PCBM)/bathocuproine (BCP)/Ag (**Figure 1(f)**), where the perovskite absorber composition is $\text{MA}_{0.65}\text{FA}_{0.35}\text{PbI}_3$ (MA is methylammonium; FA is formamidinium). Current density-voltage (J - V) characteristics and external quantum efficiency (EQE) spectra of representative devices as a function of the as-sputtered NiO_x thickness (varying from 10 to 40 nm) are shown in **Figure S1**. The spectral responses, especially in the short wavelength (< 500 nm) range, decrease upon increasing NiO_x film thickness, consistent with the trend of the transmission spectra of ITO/ NiO_x (**Figure S2**). Consequently, the short-circuit current density (J_{sc}) decreases upon increasing NiO_x thickness. In contrast, the open-circuit voltage (V_{oc}) increases with the film thickness due to the reduced leakage current at the front ITO electrode. Nonetheless, all the devices exhibit moderate performances with PCEs less than 15.3%. The limited performance of these devices is attributed to relatively low carrier density in the as-sputtered NiO_x films. The Hall effect measurement reveals that the carrier density of the as-sputtered NiO_x film is $3.84 \times 10^{11} \text{ cm}^{-3}$, substantially lower than that for the NiO_x HTLs used in efficient PSCs ($> 10^{14} \text{ cm}^{-3}$)^{9, 33-35}. Such low carrier density undoubtedly indicates a high resistivity of the as-sputtered NiO_x film. **Figure S3** presents a linear sweep voltammetry (LSV) measurement of the as-sputtered NiO_x film using two-electrode configuration, which shows a resistivity value of $1.950 \times 10^3 \Omega \text{ cm}$.

In general, most of the binary metal oxides exhibit semi-insulating properties in perfect stoichiometry. Even a slight deviation from stoichiometric composition changes the electronic structure of these oxides due to the introduction of native defects within the lattice^{36, 37}. NiO_x tends to show a p-type semi-conducting behavior as a result of the formation of nickel vacancies (V_{Ni}'')^{38, 39}. For oxygen-rich stoichiometry, two Ni^{2+} ions each lose an extra electron to maintain charge neutrality near the V_{Ni}'' site of the NiO lattice, thus contributing a quasi-localized pair of holes to form Ni^{3+} ions^{40, 41}. Then the density of localized states near the valance band increases, and the hopping transport barrier for holes reduces, resulting in an increased hole mobility and decreased resistivity³⁶. The X-ray photoemission spectroscopy (XPS) displayed in **Figure 2(a)** confirms that the as-sputtered NiO_x film has a low concentration of Ni^{3+} species. To introduce extra oxygen into the NiO_x film to promote the formation of V_{Ni}'' , which can

effectively increase the carrier density and reduce the film resistivity, a simple approach, *i.e.*, post-annealing, was employed to treat the as-sputtered NiO_x films.

The as-sputtered NiO_x films were annealed in ambient air at various temperatures. GIXRD patterns displayed in **Figure 2(b)** and **S5(a)** show that the (200) peak slightly shifts to a higher diffraction angle upon increasing the annealing temperature. This right-shifted diffraction peak corresponds to a decrease in the interplanar spacing, which indicates the formation of V_{Ni}'' and the shrink of the NiO_x lattice. **Figure S5(b)** shows that there is no obvious difference in optical transmittance of the film after the post-annealing. Atomic force microscope (AFM) images illustrated in **Figure S5(c)-S5(e)** reveal that the post-annealing doesn't influence the root-mean-squared film roughness (R_q) but makes the film denser and smoother, indicated by the decreased arithmetical mean deviation roughness (R_a). XPS was then conducted to analyze the surface stoichiometry of the annealed NiO_x films. Compared with the as-sputtered one (**Figure 2(a)**), the Ni 2p_{3/2} peak of the annealed NiO_x film at 250 °C (**Figure 2(c)**) displays a higher peak intensity of NiOOH (856.87 eV) and an extra peak located at 858.10 eV that is ascribed to the Ni₂O₃ species^{20, 30, 42}. Note that the Ni³⁺ usually comes from two species: Ni₂O₃ and NiOOH. In the as-sputtered NiO_x film we ascribed the third peak (856.87 eV) to NiOOH component because Ni₂O₃ is not stable at low temperature in ambient air. However, when annealed above 250 °C, there is enough driving force for the dehydration/dehydroxylation reaction to convert Ni(OH)₂/NiOOH to the higher order oxide (Ni₂O₃)³⁰. **Figure S6** shows more XPS spectra of the NiO_x films annealed at various temperatures. The extracted binding energies and component ratios are summarized in **Table S3**. Clearly the annealing process introduces more Ni³⁺ species into NiO_x films. Particularly, Ni₂O₃ appears when the annealing temperature is higher than 250 °C. The film resistivity and carrier density as a function of the annealing temperature were measured and plotted in **Figure 2(d)**. Hall effect measurement uncovers a continual increase of the carrier density of the annealed NiO_x films upon increasing the annealing temperature, which is consistent with the decreased resistivity determined by the LSV measurement (**Figure S7**). Note that after the 250 °C annealing, both the carrier density and conductivity of the annealed NiO_x film climb rapidly, which

is associated with the appearance of Ni_2O_3 . The carrier density of NiO_x film jumps from 3.84×10^{11} to $3.79 \times 10^{13} \text{ cm}^{-3}$, while the film resistivity reduces from 1.95×10^3 to $4.71 \times 10^2 \Omega \text{ cm}$.

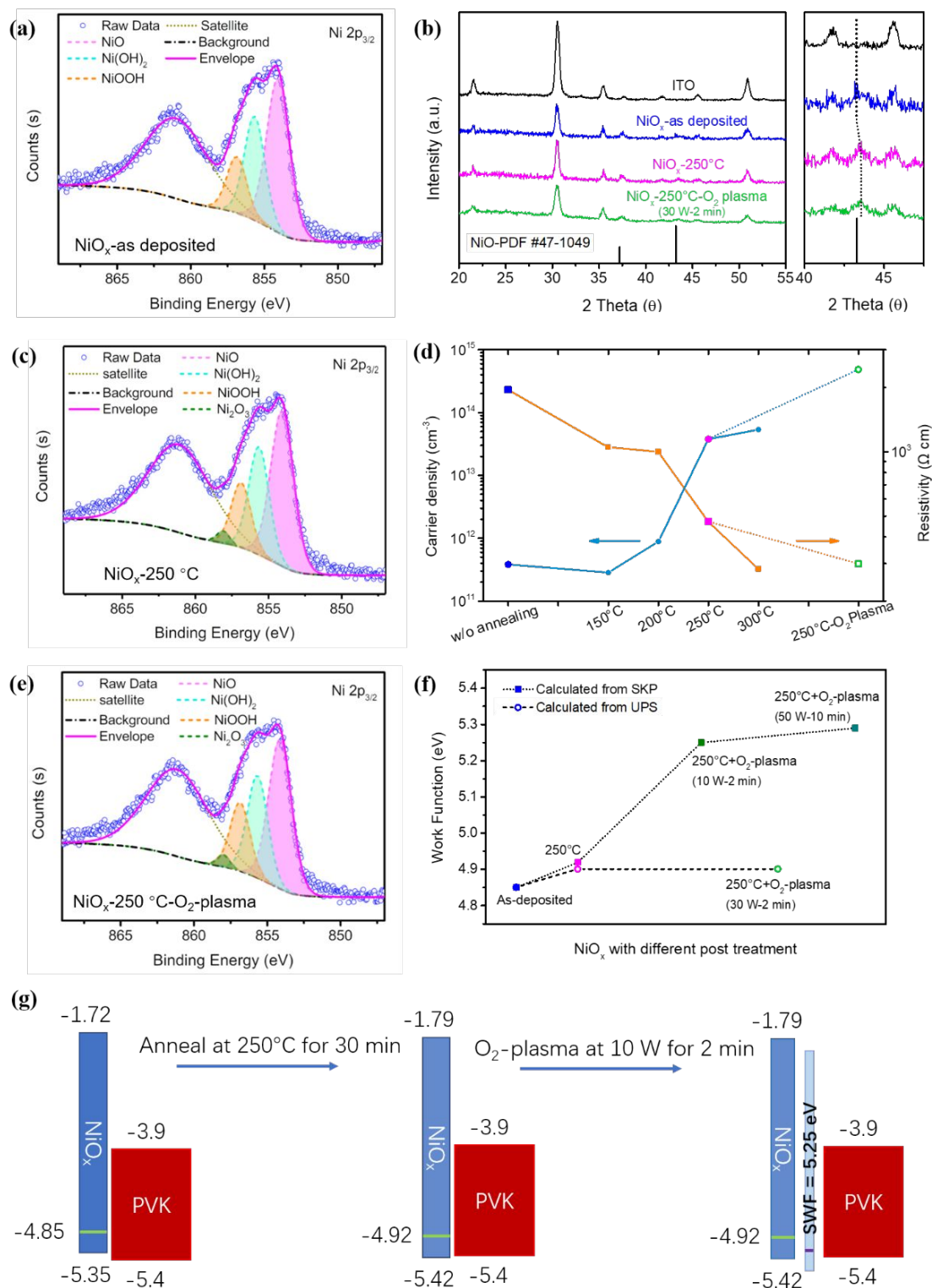


Figure 2. XPS spectra of $\text{Ni } 2p_{3/2}$ state for (a) as-sputtered NiO_x , (c) NiO_x annealed at

250 °C for 30 min, and (e) NiO_x annealed at 250 °C followed by O₂-plasma at 30 W for 2 min. (b) GIXRD patterns of the sputtered NiO films with different post treatment. ITO substrate was also shown here to facilitate comparison. (d) Carrier density and film resistivity of the NiO_x films treated with different conditions. (f) Surface work function of the various NiO_x films calculated from SKP and UPS. (g) The energy alignment schematic of different NiO_x and perovskite. SWF represents the surface work function shift after the oxygen plasma treatment.

Devices with different NiO_x film thicknesses and annealing temperatures were then fabricated to verify the feasibility of the post-annealing. **Figure S8 and S9** summarize the optimization processes of device performances. The optimal thickness and annealing temperature are found to be 20 nm and 250 °C, respectively. The J_{sc} first increases upon the annealing temperature, which is in line with the trend of film carrier density; then it decreases once the temperature further rises to 300 °C, likely due to the degradation of ITO at high temperature. However, although the annealing process improves the device performance, especially the J_{sc} , the devices still exhibit restrained PCEs of 16.6% with a moderate V_{oc} of 0.98 V.

Although the annealing process improves the carrier density of the sputtered NiO_x film significantly, it remains lower than the expected value ($>10^{14}$ cm⁻³) as we mentioned above, which is partially responsible for the limited PSC performance. And to increase the V_{oc} of PSCs, one can deepen the E_F of NiO_x to reduce the potential energy loss of hole transfer from perovskite to NiO_x and suppress the interfacial recombination through band alignment engineering^{13, 43}.

Oxygen (O₂)-plasma treatment is a widely used method to modify the surface and electrical properties of thin films. It has been demonstrated that the O₂-plasma treatment could influence the chemical stoichiometry and surface WF of NiO_x thin films, thus adjusting their carrier density and interfacial energy level alignment^{13, 30, 42, 44}. In addition to the post-annealing, we applied O₂-plasma treatment to further adjust the optoelectronic properties of the sputtered NiO_x. Considering the possible damage of O₂-plasma to the NiO_x film surface as reported in the literature^{27, 42}, a relatively low

plasma power (30 W) and a short treating time (2 min) were chosen first to explore the potential influences of the O₂-plasma treatment on the annealed NiO_x films. **Figure 2(e)** presents the XPS spectrum of the annealed NiO_x film (250 °C) with the O₂-plasma treatment. More NiOOH specie presents but the Ni₂O₃ signal changes little after the O₂-plasma treatment, compared to the film which underwent only the annealing process (**Figure 2(c)** and **Table S3**). This is consistent with the literature that the energy provided by O₂-plasma is insufficient to induce the crystallographic reorganization from the cubic (NiO) or rhombohedral (Ni(OH)₂) structure to the hexagonal crystal structure (Ni₂O₃), while the conversion from Ni(OH)₂ to NiOOH occurs more easily because NiOOH has the same rhombohedral structure as Ni(OH)₂³⁰. The increased Ni³⁺ content results in the improvement of carrier density as well as film conductivity. **Figures 2(d)** and **S10** show that after the O₂-plasma treatment the carrier density of NiO_x film further increases from 3.79×10¹³ to 4.83×10¹⁴ cm⁻³, and the resistivity decreases from 4.71×10² to 2.99×10² Ω cm.

The increased NiOOH has been reported to form a surface dipole of O-Ni-OH, shifting the NiO_x film surface work function (SWF) and reducing the leakage current and recombination at the interface^{30,36}. Scanning Kelvin Probe (SKP) measurement and UPS were then conducted to investigate the SWF variation of NiO_x films with different post treatments. All the results are summarized in **Figure 2(f)**, and the original UPS spectra can be found in **Figure S11**. The as-sputtered NiO_x film shows a relatively low WF of 4.85 eV, and it slightly shifts deep to 4.92 eV after the annealing process. A low power and short time O₂-plasma treatment further moves the WF to 5.25 eV. Increasing the plasma power and time just pushes the WF slightly to 5.29 eV, which is in line with the literature^{27,42,44}. This higher WF is induced by increasing the hole concentration at the NiO_x film surface, repelling electrons and thus lowering the interfacial recombination^{30,45}. Additionally, a high density of holes is beneficial to form a good ohmic contact with the front electrode and thus reduce the series resistance^{13,42,44}. Note that the UPS measurement cannot detect the WF change of NiO_x film after the O₂-plasma treatment, which is likely due to the surface oxygen escape in high vacuum. Even in an ambient atmosphere the resistivity of O₂-plasma treated NiO_x film recovered

to its initial value after 2 h storage (**Figure S10**), indicating the loss of NiOOH species. Similar behavior was also observed by Steirer *et al.*⁴⁴ who showed that the WF of solution-processed NiO_x films enhanced by the O₂-plasma treatment exhibited a fast decay in an inert atmosphere. **Figure 2(g)** illustrates the energy level alignments of different NiO_x films with the perovskite layers. After the post-annealing the E_F of NiO_x film becomes deeper, which reducing the valance band offset between NiO_x and perovskites. With the further O₂-plasma treatment, an oxygen-rich NiO_x surface layer with deep E_F of -5.25 eV forms, which is too close to the valance band of the perovskite. This layer may act as a good surface passivation for the perovskite absorber layer, though it may also impede the carrier transfer to some extent.

We then investigated the devices based on the annealed NiO_x films treated with different plasma powers of 10-50 W for 2 min. The representative J - V characteristics and EQE spectra are shown in **Figure S 12**. The devices show significantly improved V_{oc} (1.091 V) and fill factor (FF) (76.6%) even with the lowest power of 10 W. However, the J_{sc} dropped about 1 mA cm⁻² when compared to the device based on the annealed NiO_x without the O₂-plasma treatment (**Figure S9**). Further increase in the plasma power does not affect the V_{oc} or J_{sc} but decreases the FF gradually. The best-performing device shows a PCE of 18.15%. The enhanced V_{oc} can be explained by the downshifted Fermi level of the NiO_x film with O₂-plasma treatment. While the reduced J_{sc} is likely due to the damage on the NiO_x surface caused by the O₂-plasma treatment. The AFM image displayed in **Figure S13** reveals a fuzzy surface of the O₂-plasma treated NiO_x film, which is consistent with the literature⁴². Note that the devices with the O₂-plasma treatment shows a relatively large hysteresis (**Figure S14**), which is mainly related to the unbalanced charge carrier transport. Etching by the O₂-plasma on the NiO_x surface should be partially responsible for this hampered hole transport, and the slightly mismatched energy level alignment between NiO_x and perovskite may retard the interfacial hole extraction.

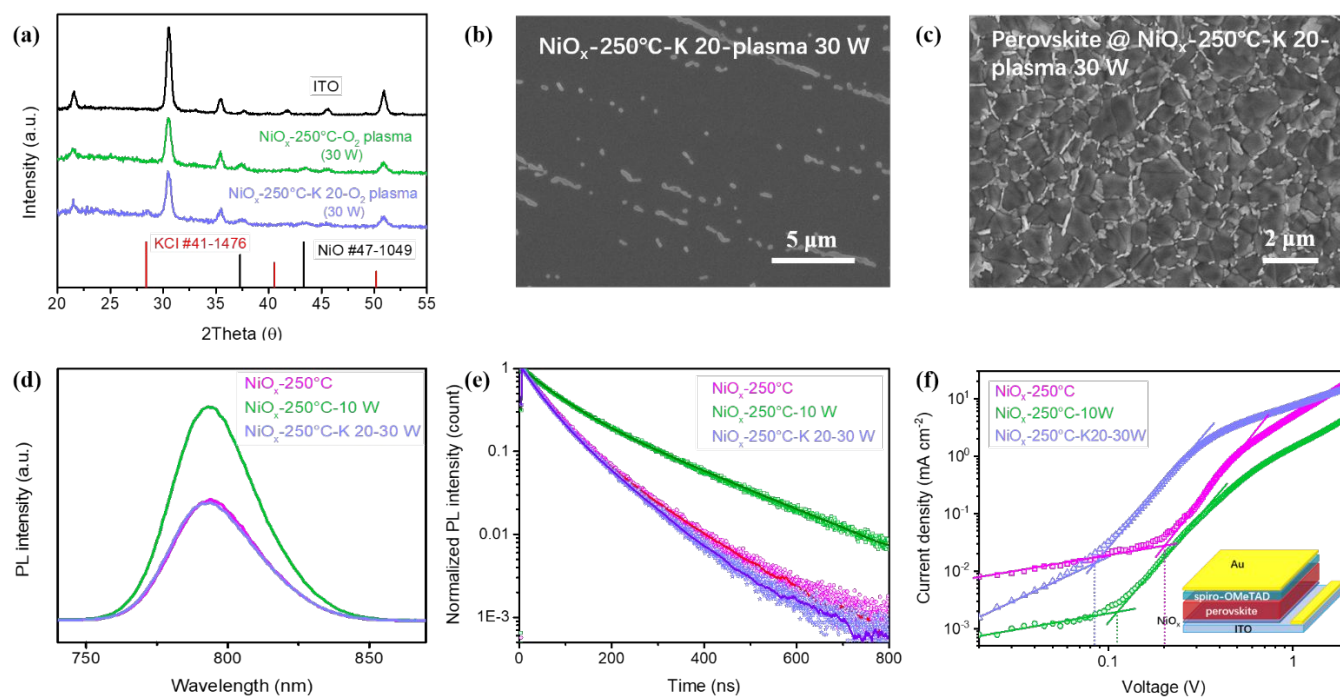


Figure 3. (a) GIXRD patterns of the annealed and O₂-plasma treated NiO_x films with and without KCl treatment. Top-view SEM image of (b) the NiO_x film treated with annealing, KCl, and O₂-plasma, and (c) the perovskite deposited on this NiO_x film. (d) Steady-state PL and (e) TRPL spectra of the perovskite deposited on three different NiO_x films. The decays were fitted with a double-exponential decay function and the obtained time constants are summarized in **Table S9**. (f) Dark J - V characteristics of the hole-only devices based on different NiO_x films. The inset shows the device structure used in the tests.

To overcome these surface imperfection issues, we adopt potassium passivation on the annealed NiO_x surface before the O₂-plasma treatment. Potassium passivation has been reported as a universal strategy to suppress the bulk and interface defects and minimize the device hysteresis^{7, 19, 28, 46, 47}. Here, we used KCl for surface passivation. The GIXRD patterns shown in **Figure 3(a)** indicate the formation of KCl crystals after spin-coating of the potassium salt solution atop the NiO_x film. The SEM image (**Figure 3(b)**) reveals a discrete distribution of KCl particles on the NiO_x surface. This discontinuous coverage of KCl at the interface was also reported by Liu *et al.*²⁸ who deposited KCl atop the SnO₂ layer. They discovered that the presence of KCl

significantly reduced the interface defects and recombination loss, with little effect on the perovskite crystal structure and electrical properties. The nearly invariable surface morphology and diffraction peaks of perovskite films deposited on NiO_x with and without KCl passivation (**Figure 3(c)** and **S15**) confirm that the KCl treatment does not affect the structural properties of the subsequently deposited perovskite films.

Devices were then fabricated to check the potassium passivation tactics. Note that the KCl treatment can influence the optimal O₂-plasma power as shown in **Figure S16**. This is understandable because a relatively strong plasma power is helpful to etch the redundant insulative Ni(OH)₂ formed during the potassium treatment using the aqueous KCl solution, thus enhancing the charge transport and collection at the perovskite/NiO_x interface. On this basis, we further investigated the effect of KCl concentration on the device performance. **Figure S17** displays the photovoltaic performance of the devices as a function of KCl concentration, including the *J-V* characteristics, EQE spectra and the corresponding steady state efficiencies. The KCl concentration seems to have very limited effect on the device performance especially for the PSCs with high plasma power (30 W) treatment. One possible reason is that the KCl particles were partially rinsed out during perovskite deposition due to the low solubility of KCl in mixed dimethyl sulfoxide (DMSO)/dimethylformamide (DMF)^{48, 49}, and the other may be originated from the etching effect of the plasma treatment (**Figure S18**). They both make the actual content of KCl in the final devices relatively low and have little discrepancy. The optimized device with 20 mg ml⁻¹ KCl plus 30 W O₂-plasma etch yields a champion PCE of 19.16%, with a *J_{sc}* of 23.27 mA cm⁻², *V_{oc}* of 1.049 V, and FF of 78.8%.

Steady-state photoluminescence (PL) and time-resolved photoluminescence (TRPL) of the perovskites deposited on different NiO_x films were then performed to identify the causes of performance improvement, and the results are illustrated in **Figure 3(d)** and **3(e)**, respectively. The measurements were made using excitation/collection through the NiO_x/perovskite interface to evaluate the behavior of charge carriers nearest to the interface. Three representative NiO_x films, treated with only thermal annealing (NiO_x-250 °C), thermal annealing plus O₂-plasma (NiO_x-250 °C-10

W), and 3-step treatment with KCl passivation (NiO_x-250 °C-K 20-30W) were selected for comparison. As a contrast, a bare perovskite film that deposited on a clean glass substrate have also been measured and shown in **Figure S19**.

The perovskite layer deposited on the NiO_x-250 °C-10 W film shows higher PL intensity and longer PL lifetime (τ_{ave}) than the one with NiO_x-250 °C film. The presence of a high SWF layer atop NiO_x surface after the O₂-plasma treatment should be partially responsible for the increased PL intensity because it retards the charge extraction from the perovskite to NiO_x. Interestingly, the sample based on NiO_x-250 °C-K 20-30W shows a similar PL intensity and lifetime compared to the post-annealed sample (NiO_x-250 °C), seemingly indicating a higher hole extraction efficiency from the perovskite to NiO_x. However, besides the charge extraction, the trap density also influences the PL emission and carrier lifetime. A high trap density in the perovskite layer and at the interface would increase the non-radiative recombination, thus decreasing the fluorescence intensity and carrier lifetime.

To further analyze the trap density in the perovskite films deposited on different NiO_x layers, we conducted the LSV measurement using hole-only devices with the structure of ITO/different NiO_x/perovskite/spiro-OMeTAD/Au. **Figure 3(f)** shows the results plotted in double logarithmic scale. The trap-state density (N_d) can be estimated by the trap-filled limit voltage (V_{TFL}), which is determined from the first kink point^{7, 50}. The V_{TFL} extracted from these devices are 0.198, 0.114, and 0.093 V for the perovskite deposited on NiO_x-250 °C, NiO_x-250 °C-10 W, and NiO_x-250 °C-K 20-30 W, respectively. The corresponding trap densities are thus calculated to be 1.49×10^{15} , 8.60×10^{14} , and 7.02×10^{14} cm⁻³. The reduced trap density in the O₂-plasma treated device (NiO_x-250 °C-10 W) is likely due to the suppressed surface defects at the NiO_x/perovskite interface, which is believed to originate from the presence of dipoles (NiOOH) on NiO_x film surface³⁰. As to the device with the KCl treatment, although the effect of O₂-plasma is likely weakened due to the introduction of KCl, the incorporation of K⁺ ions helps decreasing the defect density in the perovskite owing to the reduced iodide Frenkel defect⁵¹ and/or the formation of ordered NiO_x/perovskite interface¹⁹. The similar trap density between NiO_x-250 °C-10 W and NiO_x-250 °C-K 20-30 W

samples confirms that the faster charge extraction of the latter one is the main reason for the quicker PL quenching and shorter carrier lifetime. The combination of low trap density and fast charge extraction accounts for the excellent device performances in PSCs with the NiO_x-250 °C-K 20-30 W.

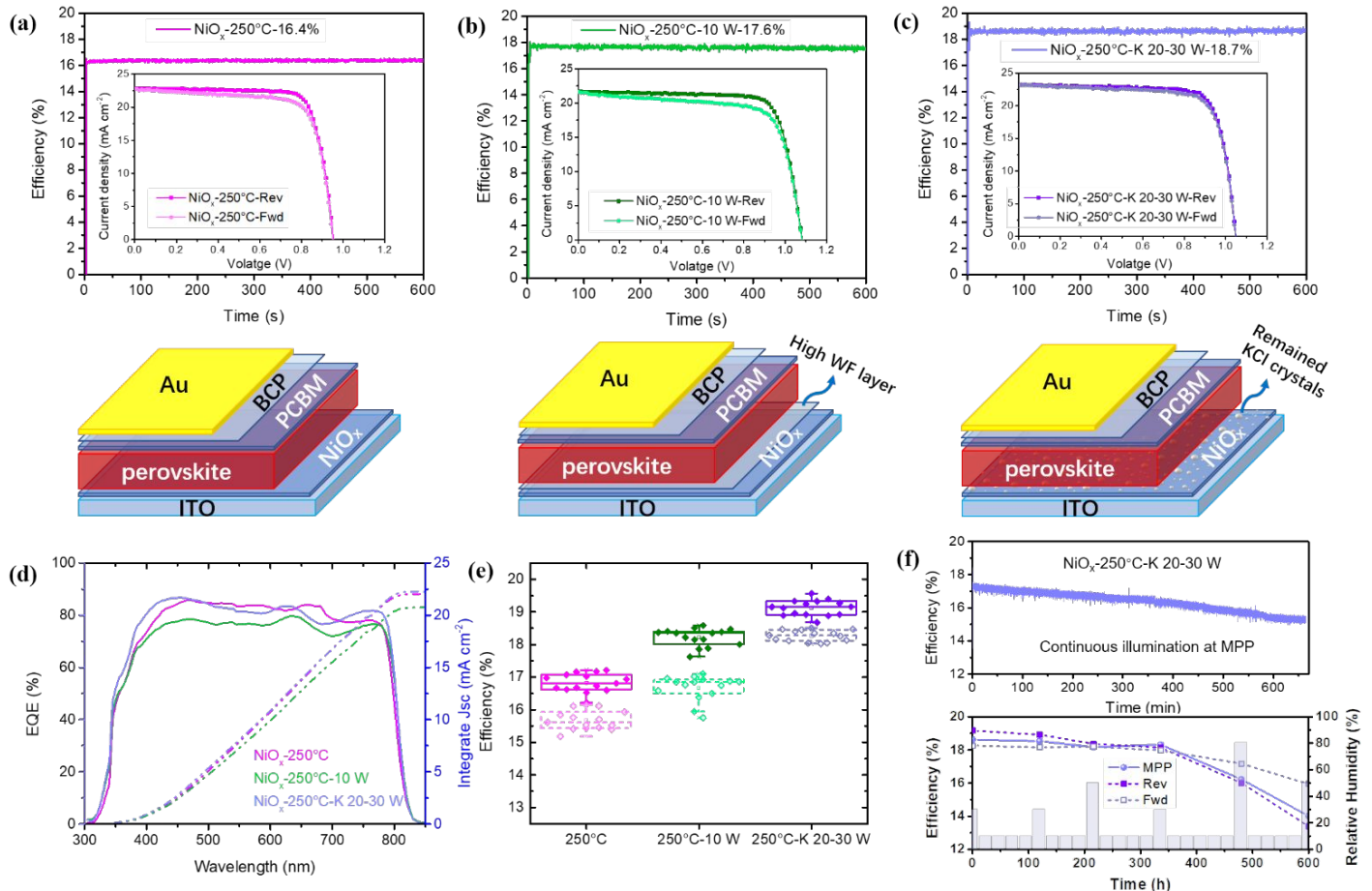


Figure 4. The J - V curves, steady-state efficiencies that tracking at maximum power point (MPP) and their corresponding device structures of the PSCs with a) NiO_x-250 °C, b) NiO_x-250 °C-10 W, and c) NiO_x-250 °C-K 20-30 W HTLs. d) EQE spectra and their corresponding $J_{integrate}$, e) Statistical distribution of these three kinds of devices. f) The illumination stability (top panel) and long-term stability (bottom panel) of the device with optimized NiO_x-250 °C-K 20-30 W HTL.

The champion device performances and their corresponding device structure with NiO_x-250 °C, NiO_x-250 °C-10 W, and NiO_x-250 °C-K 20-30 W HTLs are displayed in **Figure 4(a)-4(c)**, respectively. Clearly, the O₂-plasma treatment strikingly improves

the device V_{oc} but decreases J_{sc} with unexpected increased hysteresis. Further KCl passivation leads to the recovered J_{sc} and reduced hysteresis without sacrificing V_{oc} , resulting in the best device performance. The integrated current density ($J_{integrate}$) calculated from the corresponding EQE spectra (**Figure 4(d)**) is consistent with the J_{sc} of the best performing cell in each category. The statistical distributions of more than 15 cells for each category of devices (**Figure 4(e)**) reveals the similar PCE and hysteresis trends with the best-performing devices. The detailed photovoltaic parameter statistics including the V_{oc} , J_{sc} , FF, and PCE are presented in **Figure S20**. The best and statistic device performance of these three types of PSCs are tabulated in **Table 1**.

In addition to power conversion efficiency, stability is another important metric for evaluating PSCs. **Figure 4(f)** shows the device efficiency evolution with the optimized HTL (NiO_x-250 °C-K 20-30 W) under continuous illumination (top panel) and stored in dark and ambient air without encapsulation (bottom panel). The device maintained 88% of its initial efficiency after 660 min tracking at maximum power point (MPP) under continuous AM1.5 G solar illumination. As to the shelf lifetime test, the device was stored in a dry box and tested periodically in ambient air with a fluctuant relative humidity (RH) varying from 30 to 80%. **Figure S21** gives the detailed J - V curves and their corresponding MPP efficiencies tested at certain times, and the relevant parameters are summarized in **Table S10**. When RH is less than 50% the device shows insignificant PCE changes. However, when ambient RH is higher than 80% and the PCE drops significantly. The device only maintains 75% of its initial efficiency after 600 h aging. More interestingly, the device aging process shows a clear increase and reverse in hysteresis, which means the hysteresis index ($PCE_{Reverse\ scan} - PCE_{Forward\ scan}$) changes from positive to negative during the aging test. We speculated that this phenomenon might be related to the interdiffusion and reaction of iodine and silver ions. As time passes by, the I⁻ ions can diffuse through the electron transport layer and accumulate at the Ag inner surface and then react with it. The high humidity that helps to decompose the perovskite undoubtedly accelerates this process⁵²⁻⁵⁴. As a result, the decreased electron extraction and collection caused by the erosion of Ag and the formation of AgI barrier can significantly degrade the device performance and affect

its hysteresis behavior. Meanwhile, the diffused Ag in perovskite that may react with the perovskite and/or form the Ag metal clusters acting as recombination centers should also contribute to the degradation of device efficiency⁵⁵. Further evidences are still needed to determine the underlying reasons to avoid the device deterioration from the side of Ag electrode.

Table 1. Summary of the photovoltaic parameters of PSCs based on NiO_x-250 °C, NiO_x-250 °C-10 W, and NiO_x-250 °C-K 20-30 W HTLs.

| Sweep | | V_{oc} [V] | J_{sc} [mA cm ⁻²] | FF [%] | PCE [%] | $J_{integrate}$ [mA cm ⁻²] | MPP [%] |
|---|-----|-----------------|------------------------------------|-----------|------------|---|------------|
| NiO_x-250 °C | | | | | | | |
| Average | Rev | 0.944±0.004 | 22.81±0.18 | 0.78±0.01 | 16.83±0.28 | | |
| | Fwd | 0.942±0.004 | 22.66±0.18 | 0.74±0.01 | 15.68±0.30 | | |
| Champion | Rev | 0.953 | 22.825 | 0.789 | 17.163 | 22.03 | 16.4 |
| | Fwd | 0.950 | 22.797 | 0.744 | 16.113 | | |
| NiO_x-250 °C-10 W | | | | | | | |
| Average | Rev | 1.082±0.013 | 21.59±0.11 | 0.78±0.01 | 18.22±0.27 | | |
| | Fwd | 1.081±0.014 | 21.71±0.16 | 0.71±0.01 | 16.68±0.39 | | |
| Champion | Rev | 1.083 | 21.632 | 0.785 | 18.384 | 20.74 | 17.6 |
| | Fwd | 1.081 | 21.628 | 0.721 | 16.856 | | |
| NiO_x-250 °C-K 20-30 W | | | | | | | |
| Average | Rev | 1.049±0.004 | 23.10±0.07 | 0.79±0.01 | 19.12±0.24 | | |
| | Fwd | 1.046±0.007 | 23.16±0.10 | 0.75±0.01 | 18.27±0.17 | | |
| Champion | Rev | 1.049 | 23.170 | 0.788 | 19.158 | 22.26 | 18.7 |
| | Fwd | 1.048 | 23.214 | 0.761 | 18.510 | | |

Conclusion

In summary, we adopted a synergistic triple interface treatment combination to manipulate the optoelectronic properties of the sputtered NiO_x films and hence

improved the efficiency of the resultant PSCs. We showed that the extra oxygen introduced by the post-annealing and O₂-plasma treatment significantly increased the film conductivity and carrier density. Furthermore, the increased dipole species (NiOOH) on the NiO_x surface shifted the NiO_x SWF and thus decreased the defect recombination at the NiO_x/perovskite interface. This effect is more remarkable in the O₂-plasma treated process. Additionally, the KCl passivation process was adopted before the O₂-plasma treatment to mitigate the plasma damages on the NiO_x surface. The presence of KCl helped to improve the hole extraction efficiency from perovskite to NiO_x and thus reduced the *J-V* hysteresis. The resultant devices with the modified sputtered NiO_x HTLs delivered a highest stabilized efficiency of 18.7% with good reproducibility and stability. Our results offer an efficient strategy to adjust the bulk and surface properties of the sputtered NiO_x films and achieve high performance of the PSCs with the sputtered NiO_x as HTL.

Statement of contributions

X. Zheng and Z. Song conceived and designed this study. X. Zheng performed the experiments. C. Chen, C. Li and X. Yin helped to fabricate the devices. X. Zheng, Z. Song, Z. Chen, and S. Bista characterized the films and devices. R. Awni assisted the characterization. X. Zheng and Z. Song wrote the paper. H. Lei helped to review the primary manuscript. P. Gui and N. Shrestha helped to supplement the experiment and complete the revision. X. Zheng, Z. Song, C. Tao, R. Ellingson, Y. Yan and G. Fang reviewed and edited the final manuscript. All authors read and approved the manuscript.

Acknowledgment

This work at Wuhan University was financially supported by the National Natural Science Foundation of China (11674252), Special Funds for the Development of Strategic Emerging Industries in Shenzhen (JCYJ20170818113036217), the Science and Technology Department of Hubei Province (2019AAA020) and the Fundamental Research Funds for the Central Universities (2042019kf0317). The work at the

University of Toledo was supported by the Ohio Research Scholar Program and Air Force Research Laboratory. This publication is based on research sponsored by Air Force Research Laboratory under agreement number FA9453-18-2-0037. The U.S. Government is authorized to reproduce and distribute reprints for Governmental purposes notwithstanding any copyright notation thereon. The views and conclusions contained herein are those of the authors and should not be interpreted as necessarily representing the official policies or endorsements, either expressed or implied, of Air Force Research Laboratory or the U.S. Government. X. Z. acknowledges the financial support from China Scholarship Council (CSC, No. 201806270094).

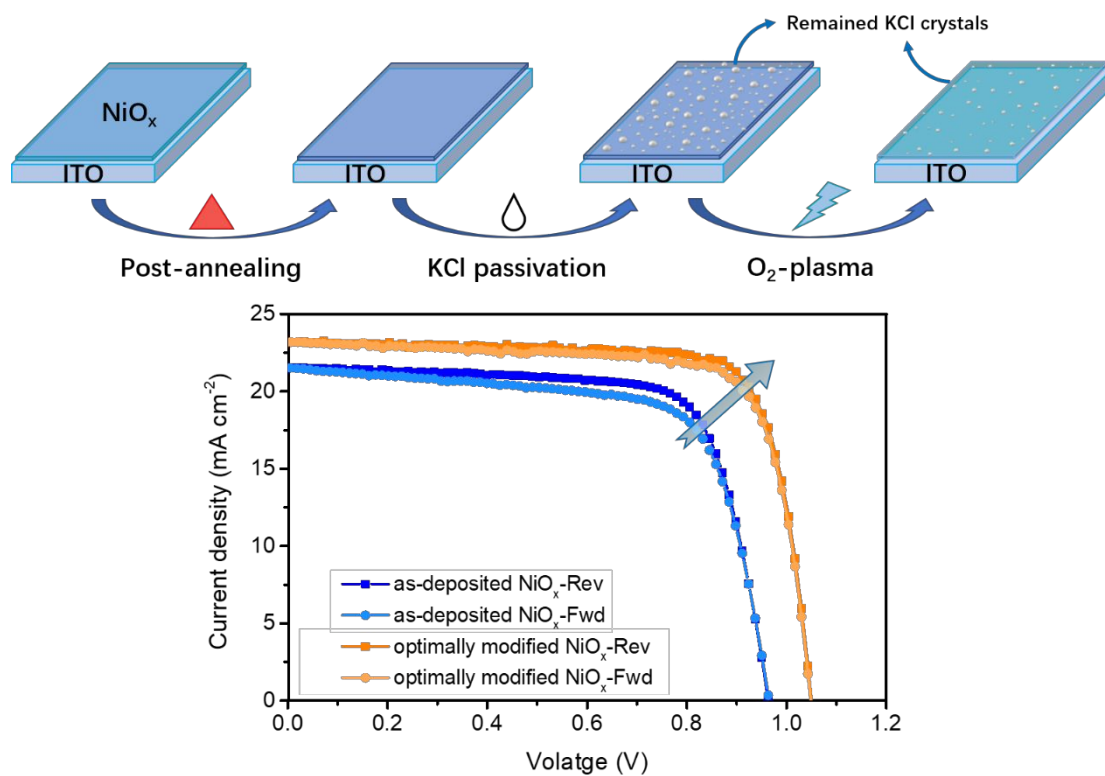
Notes and References

1. M. M. Lee, J. Teuscher, T. Miyasaka, T. N. Murakami and H. J. Snaith, *Science*, 2012, **338**, 643-647.
2. G. Xing, N. Mathews, S. Sun, S. S. Lim, Y. M. Lam, M. Gratzel, S. Mhaisalkar and T. C. Sum, *Science*, 2013, **342**, 344-347.
3. W. J. Yin, T. Shi and Y. Yan, *Adv. Mater.*, 2014, **26**, 4653-4658.
4. <https://www.nrel.gov/pv/assets/pdfs/best-research-cell-efficiencies.20190703.pdf>.
5. H.-L. Chen, Y.-M. Lu and W.-S. Hwang, *Surf. Coat. Technol.*, 2005, **198**, 138-142.
6. G. Li, Y. Jiang, S. Deng, A. Tam, P. Xu, M. Wong and H. S. Kwok, *Adv Sci*, 2017, **4**, 1700463.
7. X. Yin, J. Han, Y. Zhou, Y. Gu, M. Tai, H. Nan, Y. Zhou, J. Li and H. Lin, *J. Mater. Chem. A*, 2019, **7**, 5666-5676.
8. N. Sun, G. Fang, P. Qin, Q. Zheng, M. Wang, X. Fan, F. Cheng, J. Wan and X. Zhao, *Sol. Energy Mater. Sol. Cells*, 2010, **94**, 2328-2331.
9. W. Chen, Y. Wu, J. Fan, A. B. Djurišić, F. Liu, H. W. Tam, A. Ng, C. Surya, W. K. Chan, D. Wang and Z.-B. He, *Adv. Energy Mater.*, 2018, **8**, 1703519.
10. H. Zhang, J. Cheng, F. Lin, H. He, J. Mao, K. S. Wong, A. K.-Y. Jen and W. C. Choy, *ACS nano*, 2015, **10**, 1503-1511.
11. H. Zhang, X. Ren, X. Chen, J. Mao, J. Cheng, Y. Zhao, Y. Liu, J. Milic, W.-J. Yin and M. Grätzel, *Energy & Environmental Science*, 2018, **11**, 2253-2262.

-
12. Z. Liu, J. Chang, Z. Lin, L. Zhou, Z. Yang, D. Chen, C. Zhang, S. F. Liu and Y. Hao, *Adv. Energy Mater.*, 2018, **8**, 1703432.
 13. T. Wang, D. Ding, H. Zheng, X. Wang, J. Wang, H. Liu and W. Shen, *Solar RRL*, 2019, **3**, 1900045.
 14. E. Aydin, J. Troughton, M. De Bastiani, E. Ugur, M. Sajjad, A. Alzahrani, M. Neophytou, U. Schwingenschlögl, F. Laquai and D. Baran, *ACS Appl. Energy Mater.*, 2018, **1**, 6227-6233.
 15. L. Ai, G. Fang, L. Yuan, N. Liu, M. Wang, C. Li, Q. Zhang, J. Li and X. Zhao, *Appl. Surf. Sci.*, 2008, **254**, 2401-2405.
 16. S. Seo, I. J. Park, M. Kim, S. Lee, C. Bae, H. S. Jung, N.-G. Park, J. Y. Kim and H. Shin, *Nanoscale*, 2016, **8**, 11403-11412.
 17. J. H. Park, J. Seo, S. Park, S. S. Shin, Y. C. Kim, N. J. Jeon, H. W. Shin, T. K. Ahn, J. H. Noh and S. C. Yoon, *Adv. Mater.*, 2015, **27**, 4013-4019.
 18. T. Abzieher, S. Moghadamzadeh, F. Schackmar, H. Eggers, F. Sutterlütli, A. Farooq, D. Kojda, K. Habicht, R. Schmager, A. Mertens, R. Azmi, L. Klohr, J. A. Schwenzler, M. Hetterich, U. Lemmer, B. S. Richards, M. Powalla and U. W. Paetzold, *Adv. Energy Mater.*, 2019, **9**, 1802995.
 19. W. Chen, Y. Zhou, G. Chen, Y. Wu, B. Tu, F. Z. Liu, L. Huang, A. M. C. Ng, A. B. Djurišić and Z. He, *Adv. Energy Mater.*, 2019, **9**, 1803872.
 20. X. Yan, J. Zheng, L. Zheng, G. Lin, H. Lin, G. Chen, B. Du and F. Zhang, *Mater. Res. Bull.*, 2018, **103**, 150-157.
 21. A. Huang, J. Zhu, J. Zheng, Y. Yu, Y. Liu, S. Yang, S. Bao, L. Lei and P. Jin, *Journal of Materials Chemistry C*, 2016, **4**, 10839-10846.
 22. Y. Wei, K. Yao, X. Wang, Y. Jiang, X. Liu, N. Zhou and F. Li, *Appl. Surf. Sci.*, 2018, **427**, 782-790.
 23. W. Chen, F. Z. Liu, X. Y. Feng, A. B. Djurišić, W. K. Chan and Z. B. He, *Adv. Energy Mater.*, 2017, **7**, 1700722.
 24. W. Chen, Y. Wu, Y. Yue, J. Liu, W. Zhang, X. Yang, H. Chen, E. Bi, I. Ashraful, M. Grätzel and L. Han, *Science*, 2015, **350**, 944-948.
 25. A. B. Huang, J. T. Zhu, J. Y. Zheng, Y. Yu, Y. Liu, S. W. Yang, S. H. Bao, L. Lei

-
- and P. Jin, *J. Mater. Chem. C*, 2016, **4**, 10839-10846.
26. U. Kwon, B.-G. Kim, D. C. Nguyen, J.-H. Park, N. Y. Ha, S.-J. Kim, S. H. Ko, S. Lee, D. Lee and H. J. Park, *Sci. Rep.*, 2016, **6**.
27. Y. Nishihara, M. Chikamatsu, S. Kazaoui, T. Miyadera and Y. Yoshida, *Jpn. J. Appl. Phys.*, 2018, **57**, 04FS07.
28. X. Liu, Y. Zhang, L. Shi, Z. Liu, J. Huang, J. S. Yun, Y. Zeng, A. Pu, K. Sun, Z. Hameiri, J. A. Stride, J. Seidel, M. A. Green and X. Hao, *Adv. Energy Mater.*, 2018, **8**, 1800138.
29. T. Bu, J. Li, F. Zheng, W. Chen, X. Wen, Z. Ku, Y. Peng, J. Zhong, Y. B. Cheng and F. Huang, *Nat. Commun.*, 2018, **9**, 4609.
30. E. L. Ratcliff, J. Meyer, K. X. Steirer, A. Garcia, J. J. Berry, D. S. Ginley, D. C. Olson, A. Kahn and N. R. Armstrong, *Chem. Mater.*, 2011, **23**, 4988-5000.
31. S. Sajid, A. M. Elseman, H. Huang, J. Ji, S. Dou, H. Jiang, X. Liu, D. Wei, P. Cui and M. Li, *Nano Energy*, 2018, **51**, 408-424.
32. H. Wang, Y. Zhao, X. Li, C. Wu, X. Dong, Y. Ma, B. Zhang and G. Du, *Vacuum*, 2015, **119**, 77-80.
33. M. Yanagida, L. Shimomoto, Y. Shirai and K. Miyano, *Electrochemistry*, 2017, **85**, 231-235.
34. C. Chen, G. Yang, J. Ma, X. Zheng, Z. Chen, Q. Zhang and G. Fang, *J. Mater. Chem. C*, 2017, **5**, 10280-10287.
35. W. Chen, Y. Wu, Y. Yue, J. Liu, W. Zhang, X. Yang, H. Chen, E. Bi, I. Ashraful and M. Grätzel, *Science*, 2015, **350**, 944-948.
36. R. Islam, G. Chen, P. Ramesh, J. Suh, N. Fuchigami, D. Lee, K. A. Littau, K. Weiner, R. T. Collins and K. C. Saraswat, *ACS Appl. Mater. Interfaces*, 2017, **9**, 17201-17207.
37. M. A. Wittenauer and L. L. Van Zandt, *Philos. Mag. B*, 1982, **46**, 659-667.
38. J. Robertson and S. J. Clark, *Phys. Rev. B*, 2011, **83**, 075205.
39. J. A. Dawson, Y. Guo and J. Robertson, *Appl. Phys. Lett.*, 2015, **107**, 122110.
40. F. J. Morin, *Bell Syst. Tech. J.*, 1958, **37**, 1047-1084.
41. S. P. Mitoff, *J. Chem. Phys.*, 1961, **35**, 882-889.

-
42. S. Liu, R. Liu, Y. Chen, S. Ho, J. H. Kim and F. So, *Chem. Mater.*, 2014, **26**, 4528-4534.
 43. G. Yang, C. Wang, H. Lei, X. Zheng, P. Qin, L. Xiong, X. Zhao, Y. Yan and G. Fang, *J. Mater. Chem. A*, 2017, **5**, 1658-1666.
 44. K. X. Steirer, J. P. Chesin, N. E. Widjonarko, J. J. Berry, A. Miedaner, D. S. Ginley and D. C. Olson, *Org. Electron.*, 2010, **11**, 1414-1418.
 45. W. Ke, G. Fang, J. Wan, H. Tao, Q. Liu, L. Xiong, P. Qin, J. Wang, H. Lei and G. Yang, *Nat. Commun.*, 2015, **6**, 6700.
 46. T. Bu, X. Liu, Y. Zhou, J. Yi, X. Huang, L. Luo, J. Xiao, Z. Ku, Y. Peng, F. Huang, Y.-B. Cheng and J. Zhong, *Energy Environ. Sci.*, 2017, **10**, 2509-2515.
 47. M. Abdi-Jalebi, Z. Andaji-Garmaroudi, S. Cacovich, C. Stavrakas, B. Philippe, J. M. Richter, M. Alsari, E. P. Booker, E. M. Hutter, A. J. Pearson, S. Lilliu, T. J. Savenije, H. Rensmo, G. Divitini, C. Ducati, R. H. Friend and S. D. Stranks, *Nature*, 2018, **555**, 497-501.
 48. J. Dagar, K. Hirselandt, A. Merdasa, A. Czudek, R. Munir, F. Zu, N. Koch, T. Dittrich and E. L. Unger, *Solar RRL*, 2019, DOI: 10.1002/solr.201900088.
 49. R. Alexander, E. C. F. Ko, Y. C. Mac and A. J. Parker, *J. Am. Chem. Soc.*, 1967, **89**, 3703-3712.
 50. R. H. Bube, *J. Appl. Phys.*, 1962, **33**, 1733-1737.
 51. D.-Y. Son, S.-G. Kim, J.-Y. Seo, S.-H. Lee, H. Shin, D. Lee and N.-G. Park, *J. Am. Chem. Soc.*, 2018, **140**, 1358-1364.
 52. C. C. Boyd, R. Cheacharoen, K. A. Bush, R. Prasanna, T. Leijtens and M. D. McGehee, *ACS Energy Lett.*, 2018, **3**, 1772-1778.
 53. Y. Kato, L. K. Ono, M. V. Lee, S. Wang, S. R. Raga and Y. Qi, *Adv. Mater. Interfaces*, 2015, **2**, 1500195.
 54. J. Li, Q. Dong, N. Li and L. Wang, *Adv. Energy Mater.*, 2017, **7**, 1602922.
 55. M. Liu, Z. Chen, Y. Yang, H.-L. Yip and Y. Cao, *J. Mater. Chem. A*, 2019, **7**, 17324-17333.



Highlight: An appropriately combined triple interface modification, *i.e.*, post-annealing, O₂-plasma, and KCl treatments, is employed to ameliorate the optoelectronic properties of the sputtered NiO_x films and achieve better device performance.